High-throughput computational exploration of ternary M_3A_2X phases: Stability, properties, and exfoliation potential

Dandan Li,[1] Qianku Hu,[1,*] Qinghua Wu,[1] Yukai Chang,[1] Junkai Wang,[1] Qixun Xia,[1] Libo Wang,[1] Aiguo Zhou,[1,†] and Huachun Yang[2,‡]

[1]*Henan Key Laboratory of Materials on Deep-Earth Engineering, School of Materials Science and Engineering, Henan Polytechnic University, Jiaozuo 454003, China*

[2]*Do-Fluoride New Materials Co., Ltd, Jiaozuo 454000, China*

(Received 1 March 2025; revised 1 July 2025; accepted 9 July 2025; published 12 August 2025)

M_3A_2X phase is a type of ternary layered *MAX*-phase-like materials. To date, only four stable M_3A_2X phases have been discovered. In this research, high-throughput density functional theory calculations were employed to systematically identify stable M_3A_2X phases and then predict their properties. Starting from 240 possible compositions and 51 structural models for each composition, 12 M_3A_2X phases successfully passed three rounds of stability assessment (thermodynamic, dynamic, and mechanical stabilities) and thus are stable. Crystal structures of stable Sc_3S_2C, Y_3S_2C and Y_3Se_2C are novel and different from those of synthesized M_3A_2X phases. The electrical conductivities of the 12 M_3A_2X phases are generally superior to those of corresponding classic M_2AX phases, while their mechanical properties are slightly inferior. Through the comparison of bond strengths using the crystal orbital Hamilton population analysis, it has been discovered that M_3A_2X phases have a greater tendency to exfoliate into 2D MXenes than M_2AX phases. Among them, the Zr_3Se_2C, Zr_3S_2C, and Sc_3S_2C phases exhibit the highest exfoliation potential. This study provides a comprehensive understanding of M_3A_2X phases, laying a solid foundation for future experimental synthesis and technological applications.

DOI: 10.1103/stpc-qkpy

I. INTRODUCTION

MAX phases are a large family of ternary layered compounds with a general chemical formula $M_{n+1}AX_n$ ($n = 1$, 2, 3), where M represents an early transition metal, A denotes an A-group element (primarily groups 13–16 in the periodic table), and X indicates C or N [1]. These compounds exhibit a nanolaminated architecture (see Fig. 1), characterized by $M_{n+1}X_n$ layers interspersed with A-atom layers. The robust covalent M-X bonds are responsible for ceramic-like properties such as high stiffness, excellent chemical resistance, and low thermal expansion coefficients [1–4]. In contrast, the relatively weaker M-A bonds endow the material with superior thermal and electrical conductivity, enhanced damage tolerance, thermal shock resistance, and good machinability [1–4].

Two *MAX* phases (Ti_2SC and Zr_2SC) were first synthesized in 1960 [5]. Subsequently, Nowotny and co-workers reported more than 30 *MAX* phases including Ti_2AlN, V_2AlC, Zr_2InN, and Nb_2InC [1]. Since Barsoum synthesized the dense Ti_3SiC_2 phase in 1996 and highlighted its outstanding properties, *MAX* phases have gradually attracted increasing research interest [6,7]. Especially since 2011, when two-dimensional (2D) MXene was first produced by etching *MAX* phases [8], the synthesis of new *MAX* phases has gained greater practical significance. Since 2019, more than 170 new *MAX* phases (including solid solutions) have been discovered [4]. Notably, in 2023 alone, 69 new *MAX* phases were identified [4]. Currently, at least 342 *MAX* phases (including 124 ternary stoichiometric ones) have been successfully synthesized [4].

One important direction for developing new *MAX* phases is to expand the range of M, A, and X elements. A so-called top-down approach (including molten salt method and elemental exchange reaction) through substitution of the A layers is employed to synthesize new *MAX* phases. Using the molten salt substitution method, Huang's group identified new *MAX* phases with A = Fe, Co, Ni, Cu, and Zn elements [9–13]. Thin films of *MAX* phases containing noble metals have been achieved through thermally induced exchange reactions by replacement of Al, Si, and Ga with Au or Ir [14–17]. Furthermore, *MAX* phases with A = Se and Te have been reported [18–21]. In the past two years, spark plasma sintering has been used to successfully obtain a series of new *MAX* phases with Ga, Pb, In, Sb, and Cd as the A element [22–26]. Recently, *MAX* phases with boron as the X element have also been discovered experimentally [18,21,27–30].

Expanding the structural diversity of *MAX* phases is also a crucial approach to developing novel phases. Crystal structures of the classic $M_{n+1}AX_n$ phases with $n = 1$, 2, 3 exhibit a hexagonal crystal system with a $P6_3/mmc$ space group, which are presented in Fig. 1. The crystal structures in these classic *MAX* phases consist of only one A layer inserted between adjacent $M_{n+1}X_n$ blocks. In 2015 the successful synthesis of Mo_2Ga_2C marked the beginning of *MAX* phases with double A layers, in which two Ga layers

*Contact author: hqk@hpu.edu.cn
†Contact author: zhouag@hpu.edu.cn
‡Contact author: dfd0007@dfdchem.com

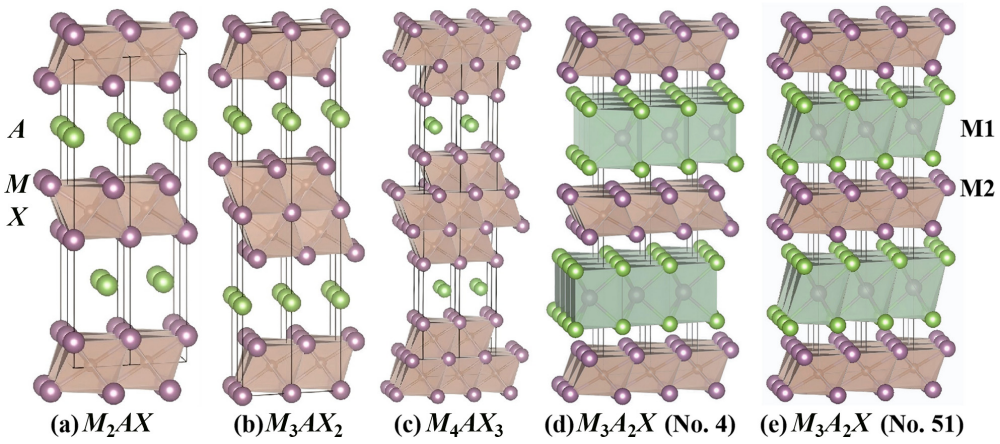

FIG. 1. Crystal structures of (a) M_2AX, (b) M_3AX_2, (c) M_4AX_3, (d), and (e) M_3A_2X phases.

exist between the neighboring Mo_2C blocks. To date, four *MAX* phases of $Ti_3Cd_2C_2$ [13], $Ti_3Au_2C_2$ [14,15], Ti_2Au_2C [15], and Nb_2Bi_2C [13] with double A layers have also been synthesized. Recently, Chen *et al.* synthesized a new series of Nb_3As_2C, V_3As_2C, Nb_3P_2C, and Ta_3P_2C *MAX* phases using molten-salt sintering and solid-state synthesis methods [31,32]. These phases have the chemical formula of M_3A_2X, which is different from traditional $M_{n+1}AX_n$. Figure 1(d) shows the crystal structure of the synthesized M_3A_2X phase. The distinguishing feature in M_3A_2X crystal structure is the insertion of an *A*-*M*-*A* block, rather than a single or double *A*-layer, between neighboring *M*-*X*-M blocks. The novel structure has brought about changes in performance. The average linear thermal expansion coefficients of M_3A_2X phases are measured as the lowest among the reported values of *MAX* phases [33]. The experimental bulk modulus of Nb_3As_2C reaches up to 225 GPa [31], close to the highest values observed in *MAX* phases [34]. Elastic, thermal, and lattice dynamic properties of these four M_3A_2X phases were also investigated through first-principles calculations [35].

To date, 67, 15, and 7 stoichiometric members have been synthesized for the classic M_2AX, M_3AX_2, and M_4AX_3 phases, respectively [4]. For the M_3A_2X phases, only the four phases mentioned above have been synthesized. It is anticipated that more stable M_3A_2X phases can be discovered through expanding the range and/or considering more combinations of the *M*, *A*, and *X* elements. The combination of numerous *M*, *A* and *X* elements will result in a large number of M_3A_2X candidates. It is impractical to evaluate the potential of large M_3A_2X candidates through experimental methods. High-throughput calculations [36] are a powerful tool for screening and identifying stable phases from a vast number of hypothetical candidates with similar crystal structures. This approach has proven successful in predicting new stable M_2AX, M_3AX_2, and M_4AX_3 phases [4,37–44]. For example, Ashton *et al.* screened a total of 3140 pure M_2AX phases and their solid solutions that can be easily synthesized in experiments from 10 530 candidates [39]. Similar work has also been done by Ohmer and colleagues, who identified 82 stable M_2AX phases from 1080 possible compositions [44]. Except for identifying stable M_2AX phases, high-throughput searches based on first-principles calculations were also conducted on M_3AX_2 and M_4AX_3 phases [4,40], as well as the solid solution *MAX* phases [43].

Given that only 4 M_3A_2X phases have been synthesized so far, there is a demand for more stable M_3A_2X compositions. In this study, we employed a high-throughput computational method to systematically predict and identify stable phases in M_3A_2X. The electrical and mechanical properties of the predicted stable M_3A_2X phases were determined and compared with those of traditional M_2AX phases. Finally, the possibility of exfoliating the M_3A_2X phases into 2D MXenes was evaluated, which could guide the M_3A_2X materials for specific applications.

II. COMPUTATIONAL DETAILS

First-principles calculations based on density functional theory (DFT) [45,46] were employed, as implemented within the Vienna Ab-initio Simulation Package (VASP) [47]. In structure relaxation, full optimization was adopted, meaning that both the atomic positions and lattice constants were relaxed simultaneously. The generalized gradient approximation (GGA), parameterized by Perdew-Burke-Ernzerhof (PBE), was taken to calculate the exchange and correlation energy of electrons. The electron-ion interaction was processed by the projector augmented wave (PAW) method [48,49] with an energy cutoff of 520 eV. The first Brillouin zone integration used the special K-point method in the form of Monkhorst-Pack (MP) [50] with a K-point accuracy of $2\pi \times 0.03$ Å^{-1}. The convergence accuracy of the iteration in the self-consistent field (SCF) of the electronic step was 1.0×10^{-5} eV/atom, and the conjugate gradient algorithm (CG) was employed for ion optimization with an energy convergence criterion of 1.0×10^{-4} eV/atom. The phonon spectrum was calculated using the finite displacement method, which was a joint calculation performed by VASP and PHONOPY software [51,52]. The Gibbs free energies at finite temperature was obtained by the quasi-harmonic approximation (QHA) method through VASP-PHONOPY. The elastic constants were calculated using the stress-strain method [53]. The crystal orbital Hamilton population (COHP) analysis was carried out using the LOBSTER code [54]. The competing phases considered herein are sourced from the

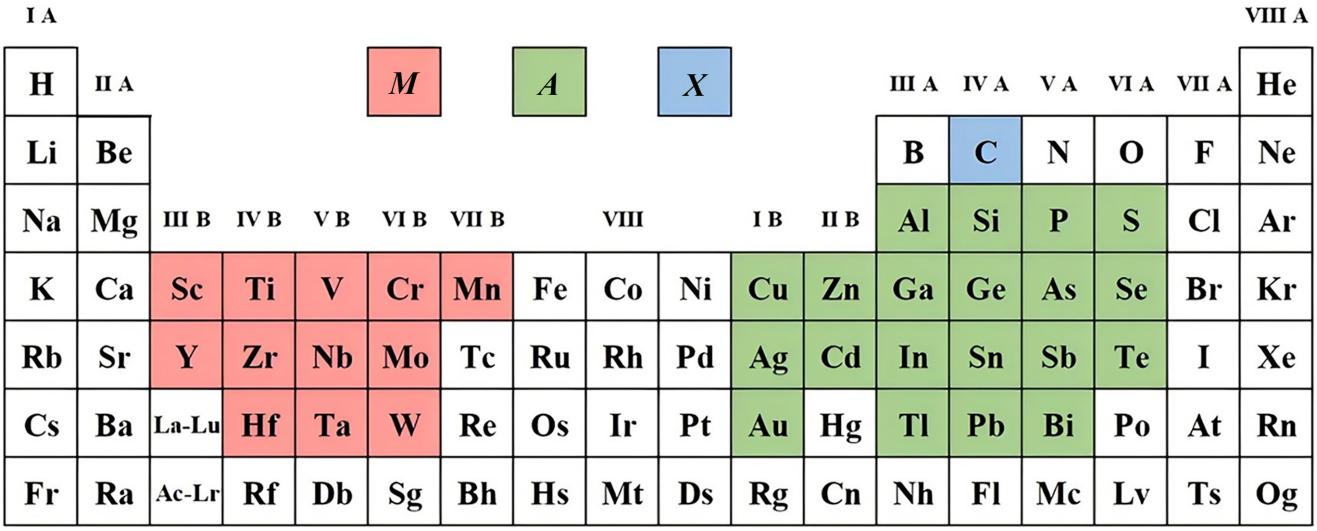

FIG. 2. Elements considered for M, A, and X atoms in the M_3A_2X phases.

Materials Project [55] and the Open Quantum Materials Database (OQMD) [56,57], which were reoptimized in this paper to get accurate energies.

III. RESULTS AND DISCUSSION

A. Elemental selection and structural model

Both the common elements present in classic *MAX* phases and the new elements found in the *MAX* phases reported recently [10,14–17,58] were considered. The element search space with 12 M elements (Sc, Ti, V, Cr, Mn, Y, Zr, Nb, Mo, Hf, Ta, W) and 20 A elements (Al, Si, P, S, Cu, Zn, Ga, Ge, As, Se, Ag, Cd, In, Sn, Sb, Te, Au, Tl, Pb, Bi) is depicted in Fig. 2. Since binary metal nitrides act as robust and stable competing phases [38], the number of stable *MAX* phases with $X = N$ is significantly smaller compared to those with $X = C$ [4]. In this work, we restrict the X element to carbon only. With this combination of elemental components, there are $12 \times 20 \times 1 = 240$ possible M_3A_2X compositions.

Although the four synthesized M_3A_2X phases share the same structure [Fig. 1(d)], it remains questionable whether the 240 M_3A_2X compositions would exhibit the same structure. Actually polymorphism phenomenon has been observed in some *MAX* phases, such as Ti_4GaC_3 [59], Ta_4AlC_3 [60], and Mo_2Ga_2C [61–63]. Thus in this paper, we investigated various crystal structures for each M_3A_2X composition. First, a 12-atom unit cell containing two M_3A_2X chemical formulas was adopted, which is commonly seen in classic *MAX* phases. Second, three stacking models along the c direction of adjacent *M-X-M* blocks, namely, I, II, and III [depicted in Fig. 3(a)], were taken into account. Third, considering different positions of A and M atoms of *A-M-A* block in the *a-b* plane, four models [shown in Fig. 3(b)] of a *A-M-A* block can be constructed: (1) The A, M, and A atoms occupy the same position, forming a straight chainlike structure. (2) One A atom and the M atom share the same position, while the other A atom occupies a different position, resulting in the A atoms forming a tetrahedral structure, with the M atom locating at the center, (3) When the A atoms in the upper and lower layers occupy the same position, they form a trigonal prism, with the M atom locating at the center, (4) In the case where the A, M, and A atoms occupy different positions, the A atoms form an octahedral structure, with the M atom at the center. Last, we positioned each of the four *A-M-A* models at different locations between adjacent *M-X-M* blocks of the three stacking models in Fig. 3(a). This process yielded a total of 81 M_3A_2X configurations. After carefully examining the 81 configurations, 30 of them had atomic arrangements identical to those of others. Therefore, there are actually only 51 distinct configurations, which were presented in Fig. S.1 (see the Supplemental Material [64]). The quantities of each type of M_3A_2X configurations, which were formed by combining the four *A-M-A* models with the three *M-X-M* stacking models, are presented in Fig. 3(c).

B. Lowest-energy configuration

All 51 crystal structures for each of the 240 possible M_3A_2X compositions were fully relaxed. A total of $240 \times 51 = 12\,240$ structural optimization calculations were thus carried out. Because atoms were positioned at highly symmetric sites in each of the 51 constructed structures, all initial structures maintained their original configurations after optimization and only minor adjustments were made to atomic positions to optimize interatomic distances.

The lowest-energy configuration of each M_3A_2X composition is the most stable thermodynamically, which is summarized in Fig. 4, and the detailed information about structure and energy is presented in Table S.1 [64]. It can be found that the model-II stacking of *M-X-M* block, as well as the chainlike and tetrahedral structures of *A-M-A* block, are unfavorable for all M_3A_2X compositions (except for Sc_3Cu_2C). Nearly half (118 out of 240) of the M_3A_2X phases have their lowest-energy structure in the form of the No. 4 configuration in Fig. S.1 [64]. The A element in these 118 M_3A_2X phases is mainly found in the main groups. The lowest-energy structure of all four synthesized M_3A_2X phases (Nb_3As_2C, V_3As_2C, Nb_3P_2C, and Ta_3P_2C) falls into this configuration, which is in accordance with previous experimental results [31]. The second most lowest-energy structure is the

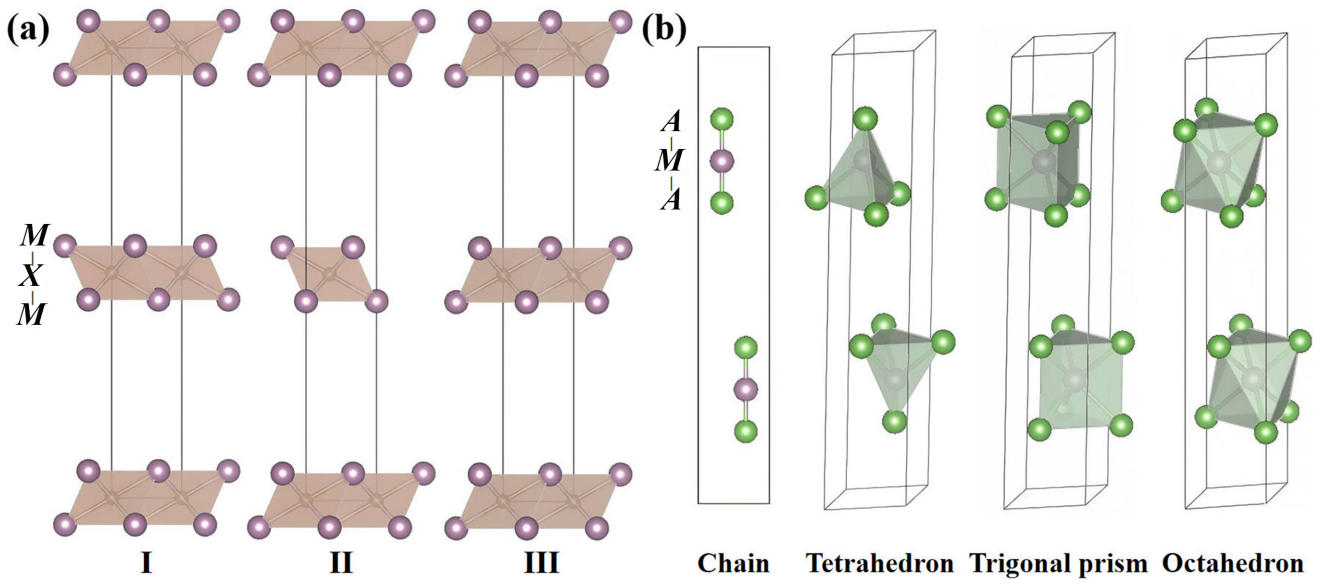

(c)

A-M-A / *M-X-M*	Chain	Tetrahedron	Trigonal prism	Octahedron
I	3 ($P6_3/mmc$)	6 ($P\bar{3}m1$)	6 ($P6_3/mmc$)	3 ($P\bar{3}m1$)
II	3 ($P3m1$)	6 ($P3m1$)	6 ($P3m1$)	3 ($P3m1$)
III	2 ($P\bar{3}m1$)	6 ($P\bar{3}m1$)	3 ($P\bar{3}m1$)	4 ($P\bar{3}m1$)

FIG. 3. (a) Three stacking models of the *M-X-M* block. (b) Four models of the *A-M-A* block. (c) Quantities of each type of M_3A_2X configurations. The corresponding space group is shown in the parentheses.

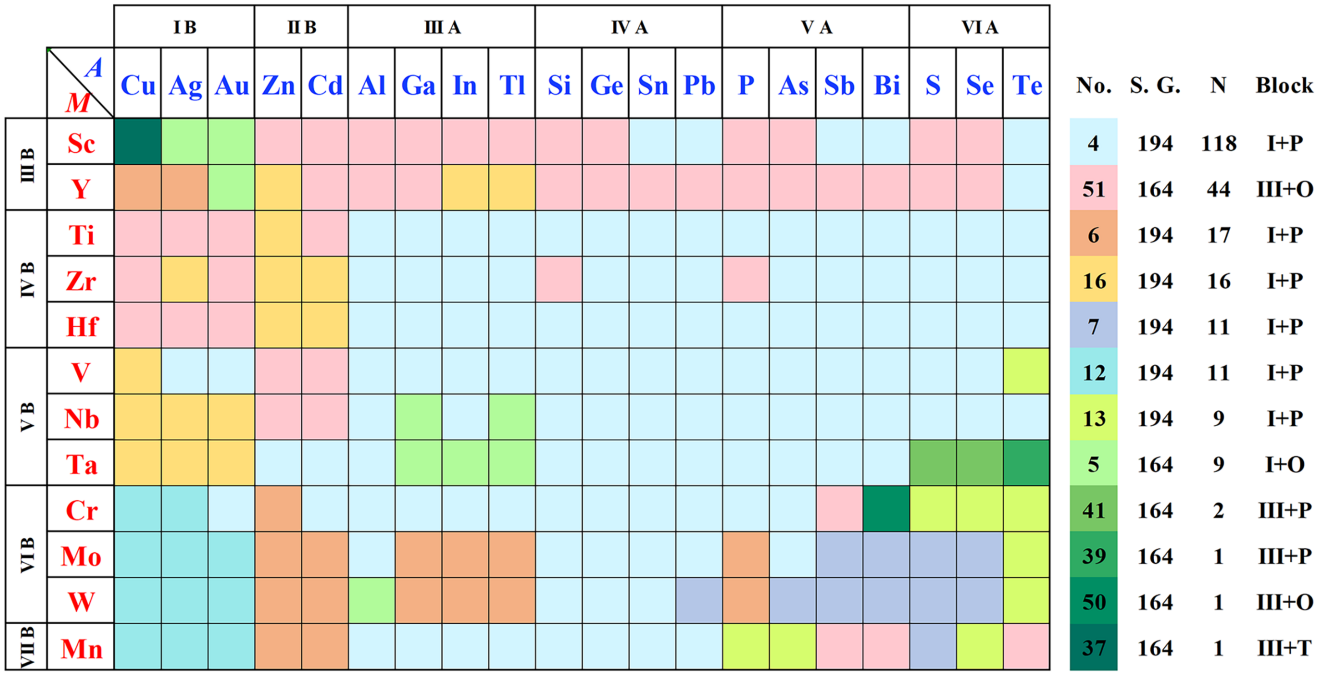

No. : ID number of structure S. G. : Space group (194 = $P6_3/mmc$, 164 = $P\bar{3}m1$) N : Number of the lowest-energy configurations

Block : M-X-M: I, III; A-M-A: Tetrahedron (T), Trigonal prism (P), Octahedron (O)

FIG. 4. Distribution and statistics of the lowest-energy configuration of each M_3A_2X composition.

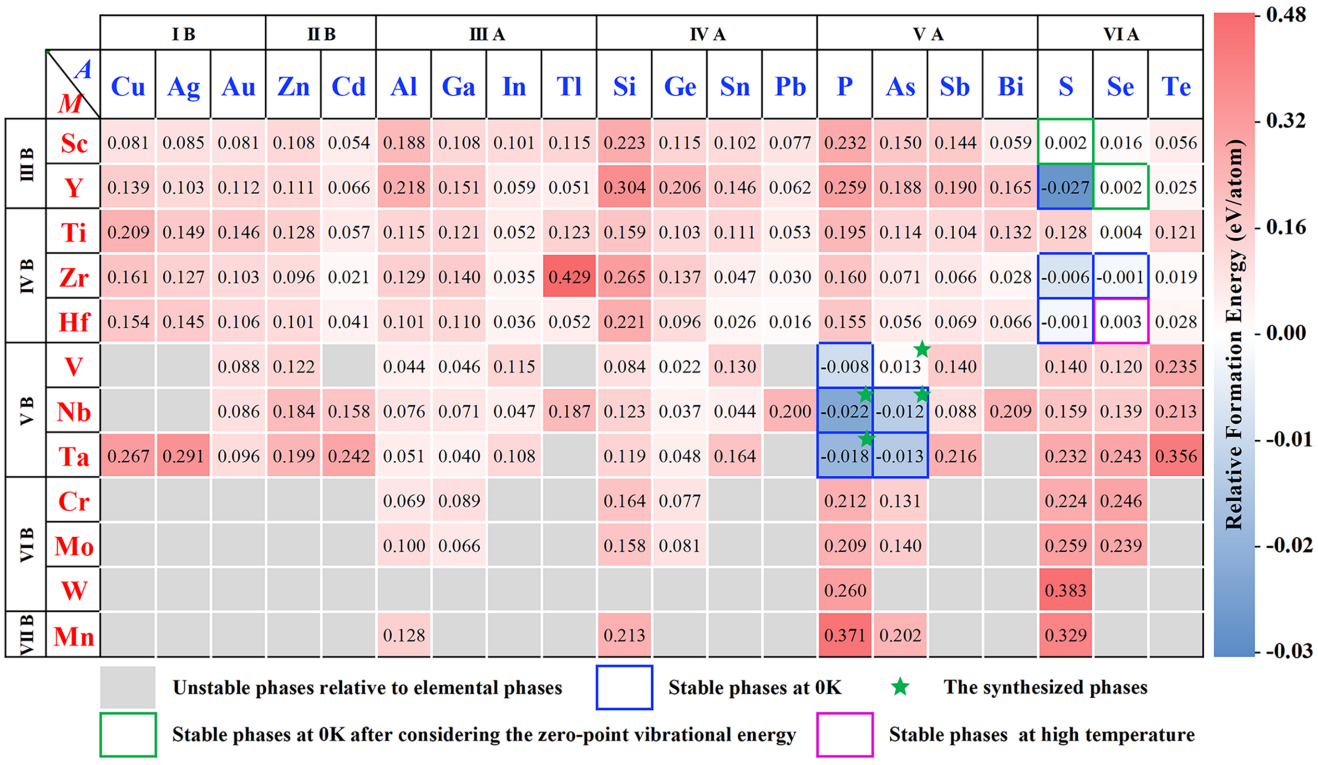

FIG. 5. Heatmaps of the formation energies E_{comp} of M_3A_2X phases relative to all competing phases. The gray boxes represent unstable phases relative to elemental phases. Thermodynamic stability of M_3A_2X phases is marked with different colors and symbols.

No. 51 configuration in Fig. S.1 [64], which is primarily found where the M element is from Group IIIB and the A element is from a transition metal group. Over half of the M_3A_2X phases do not have the experimentally synthesized No. 4 configuration as their lowest-energy structure. This validates the necessity of the methodology which involves taking various structures into account during identifying the lowest-energy structure.

The No. 4 and 51 configurations account for more than two-thirds of the lowest-energy structures. These two crystal structures are given in Figs. 1(d) and 1(e). Other configurations with smaller proportions are not described in detail here. The No. 4 configuration belongs to the $P6_3/mmc$ space group, which is formed by placing the *A-M-A* edge-sharing trigonal prism into the *M-X-M* stacking model-I. The No. 51 configuration possesses the $P\bar{3}m1$ space group and is formed through the combination of the *M-X-M* stacking model-III and the *A-M-A* edge-sharing octahedron.

C. Phase stability

The stability of the lowest-energy configurations for the 240 M_3A_2X compositions was assessed through the next three rounds: thermodynamic stability, dynamic stability, and mechanical stability.

1. Thermodynamic stability

The calculation of thermodynamic stability is crucial for discovering novel phases. Thermodynamic stability evaluates a compound's resistance to decomposition into any combination of elemental, binary, or other ternary phases, thus the candidate compound should possess a lower energy than any combination of all potential competing phases. For ternary compounds like M_3A_2X, there can be numerous combinations of competing phases. Especially for 240 M_3A_2X compositions in this work, it should take considerable time and effort to investigate the thermodynamic stability against all competing phases. Thus as an initial screening, we first investigated the thermodynamic stability of these 240 M_3A_2X compositions against their constituent elemental phases.

The formation energy of a M_3A_2X phase against its constituent elemental phases is calculated by the equation $E_f = 6E(M_3A_2X)–3E(M)–2E(A)–E(X)$, where $E(M_3A_2X)$ is the total energy (in eV/atom) of the M_3A_2X phase, and *E(M)*, *E(A)*, and *E(X)* are the total energy (in eV/atom) of the *M*, *A*, and *X* elemental phases in their ground-state bulk structures. A negative E_f value indicates the M_3A_2X phase is thermodynamically stable against decomposition into the *M*, *A*, and *X* elemental phases. The calculated E_f values of the 240 M_3A_2X compositions are summarized in Table S.2 [64]. We predict 68 M_3A_2X compositions with positive E_f values to be thermodynamically unstable. These unstable M_3A_2X phases (illustrated in Fig. 5) are primarily observed for the *M* atom in the VIIB and VIB groups (especially when the *A* atom in the 6th period). The reason behind the instability will be discussed later in this paper.

Subsequently, thermodynamic stability of the remaining 172 M_3A_2X compositions was assessed by calculating their formation energies E_{comp} relative to all competing phases using the equation $E_{comp} = E(M_3A_2X) - E$(set of the most competing phases), where $E(M_3A_2X)$ is the total energy of M_3A_2X phase and *E*(set of the most competing phases) is

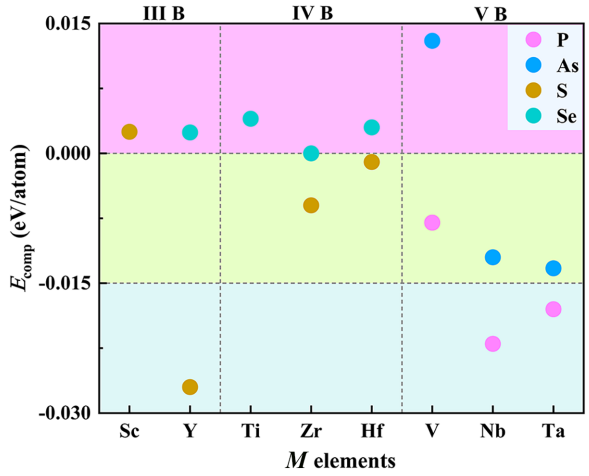

FIG. 6. E_{comp} values of nine stable and five metastable M_3A_2X phases.

the total energy of the set of the most competing phases with the same stoichiometry as the M_3A_2X phase. Identifying the set of the most competing phases out of all competing phases is the crucial step. In this paper, the set of the most competing phases, referred to as equilibrium simplex, is determined through a linear optimization procedure [38,65]. This approach has been demonstrated to be effective in both validating experimentally known *MAX* phases and predicting the existence of new ones [38–41,43,65–68].

The calculated E_{comp} values and the set of the most competing phases of the 172 M_3A_2X phases are listed in Table S.3 [64]. A heatmap (Fig. 5) of the calculated E_{comp} can visually display the stability distribution of M_3A_2X phases. Only nine M_3A_2X phases (V_3P_2C, Nb_3P_2C, Nb_3As_2C, Ta_3P_2C, Ta_3As_2C, Y_3S_2C, Zr_3S_2C, Zr_3Se_2C, and Hf_3S_2C) have negative E_{comp} and are therefore thermodynamically stable. From the values of the E_{comp} and the distribution of the stable phases, it can be seen that the stability of the M_3A_2X phases has a local characteristic and is related to the positions of the M and A atoms. The nine M_3A_2X phases are mainly distributed in two regions. One is formed when the M atom is a group-VB element (V, Nb, Ta) and the A atom is a P or As element in the VA group. Another region of stable M_3A_2X phases located near the upper right corner is formed by M = Y, Zr, and Hf and A = S and Se. According to radius ratio rule in chemistry, the radius ratio of M to A atoms plays a significant role in the stability of the *A*-*M*-*A* octahedron and prism in Figs. 1(d) and 1(e). Some papers also report that the valence electron and atomic size of the elements are major factors for the stability of *MAX* phases [39,40,44,69]. Thus, only the M_3A_2X phases with appropriate M and A atoms are stable.

The E_{comp} value (i.e. the distance to convex hull) of a compound can be thought as the thermodynamic driving force for the most stable competing phase to synthesize this compound. More negative E_{comp} means an easier tendency for synthesis. The E_{comp} values of nine stable and five metastable ($0 < E_{comp} < 0.015$ eV/atom) M_3A_2X phases are illustrated in Fig. 6. The synthesized Nb_3As_2C, Nb_3P_2C, and Ta_3P_2C indeed possess relatively lower E_{comp}. In addition, the E_{comp} values of predicted Y_3S_2C and Ta_3As_2C are also relatively low and should be more readily synthesizable. In particular, Y_3S_2C has the most negative E_{comp}. Therefore, experimenters can focus on these two phases as the targets in the future.

TABLE I. Statistics about the most competing phases for the 172 M_3A_2X phases.

Competing phases	Types	Numbers	Total
Elementary phase	*M*	10	52
	A	24	
	X	18	
Binary phase	*M*-*X*	110	310
	M-*A*	199	
	A-*X*	1	
Ternary phase	*MAX* phases	61	92
	Others	31	
Total			454

Although our calculations reflect the thermodynamic stability of M_3A_2X phases at 0 K, the results still match the experimental findings quite well. Three (Nb_3As_2C, Nb_3P_2C, and Ta_3P_2C) out of four phases synthesized experimentally [31] were calculated to be thermodynamically stable, which demonstrates the reliability of our calculations. The only discrepancy is V_3As_2C. The raw materials used for the synthesis of V_3As_2C are VAs, V, and graphite powders [31]. We calculated the formation energy for the reaction $2VAs + V + C = V_3As_2C$ to be -0.172 eV/atom, indicating that this reaction path is possible. However, V_3As_2C is unstable compared to the most stable competing phase ($VAs_2 + V_2AsC + V_5As_4$, $E_{comp} = 0.013$ eV/atom). Therefore, the synthesized V_3As_2C has a tendency to decompose in thermodynamics. In fact, some unknown phases were observed in the synthesized V_3As_2C samples [31], confirming the instability of V_3As_2C.

Next, we will analyze the set of the most competing phases listed in Table S.3 [64]. For the 172 M_3A_2X phases, none of the set of the most competing phases consists solely of three elemental materials, which indicates that it is inaccurate to judge the thermodynamic stability merely using the formation energy relative to elemental materials, as reported in [4,40,70,71]. We conducted a statistical analysis (as shown in Table I) of the most competing phases for the 172 M_3A_2X phases. Among the 454 occurrences of competing phases, elemental materials appear only 52 times. In ternary competing phases, *MAX* phases occurred 61 times, and other ternary phases occurred 31 times. Binary compounds are the most frequently occurring and account for about two-thirds. Among the binary competing phases, roughly two-thirds are *M*-*A* compounds, approximately one-third are *M*-*X* compounds, and *A*-*X* compounds occur only once. Thus, binary *M*-*A* and *M*-*X* phases emerge as the main rivals competing for stability with the M_3A_2X phase.

In previous studies on predicting *MAX* phases, a common mistake was to ignore other series of *MAX* phases as competing phases. In recent years, newly synthesized or predicted *MAX* phases have been emerging continuously, and they are not promptly included in the Materials Project and OQMD databases. Therefore, in addition to the *MAX* phases in these

two databases, stable *MAX* phases reported recently [4,40,44] were manually considered as competing phases. This operation has indeed changed the stability of some M_3A_2X phases. We take the Nb_3In_2C as an example. If we consider only the phases in Materials Project and OQMD databases, Nb_3In_2C with $E_{comp} = -0.001$ eV/atom is predicted to be stable with Nb, In, and Nb_2C as the most competing phases. However, if the stable Nb_2InC phase [4] is included in the assessment of stability, Nb_3In_2C with $E_{comp} = 0.047$ eV/atom becomes unstable with Nb, Nb_2In_5 and Nb_2InC as the most competing phases. This indicates that the stability of M_3A_2X phases could be overestimated if other series of *MAX* phases are neglected as competing phases.

Given that typical synthesis of bulk *MAX* phases is conducted at around 1500 °C, the lattice vibrational effect at high temperatures is not negligible and ought to be taken into account for precise stability prediction. Thermodynamic stability at a given temperature can be determined by calculating formation energy relative to the set of the most competing phases at the same temperature. However, in most cases the set of the most competing phases at high temperatures is the same as that at 0 K [42]. Therefore, thermodynamic stability of the M_3A_2X phase at a given temperature (T) is assessed using the equation $E_{comp}(T) = E(M_3A_2X, T) - E$(set of the most competing phases, T), where $E(M_3A_2X, T)$ is the total energy of M_3A_2X phase and E(set of the most competing phases, T) is the total energy of the set of the most competing phases (the same as that at 0 K) at this temperature of T K.

The impact of temperature on stability can be twofold. Phases that were formerly stable may become unstable, while phases that were initially unstable could turn stable. When the absolute value of the formation energy ($|E_{comp}|$) of a phase gets closer to 0, there is a high probability that the stability of this phase will be altered at elevated temperatures. Vibrational and heat capacity effects at 298 K alter E_{comp} by about 0.007 eV/atom, with entropy's influence growing at higher temperatures [72]. However, these thermal impacts vary significantly between materials, and some show minimal changes [73]. We first took the eight M_3A_2X phases within the range of $|E_{comp}| < 0.010$ eV/atom as examples to investigate the influence of temperature. From the curves of calculated E_{comp} versus temperature plotted in Fig. 7, it can be observed that when the temperature increases from 0 K to 1800 K, the E_{comp} values of 7 M_3A_2X phases except Y_3Se_2C change by less than 0.010 eV/atom. This indicates that using an E_{comp} threshold of 0.010 eV/atom is sufficient for studying the effect of temperature on the stability of M_3A_2X phases. To ensure scientific rigor, we increased the tolerance of E_{comp} and ultimately set the E_{comp} threshold at 0.015 eV/atom. Seen from Fig. 6, there are six stable and five metastable M_3A_2X phases at 0 K that meet the condition of $|E_{comp}| < 0.015$ eV/atom. The curves of calculated E_{comp} versus temperature for these 11 M_3A_2X phases are plotted in Fig. 7. We noticed that all six stable phases keep steady within the entire temperature range. The Hf_3Se_2C becomes stable when the temperature is higher than around 1000 K. V_3As_2C and Ti_3Se_2C remain unstable during the whole temperature range. After considering only the zero-point vibrational energy, the formation energies of Sc_3S_2C and Y_3Se_2C shift from positive to negative, making them the ground-state stable phases at 0 K. However, the

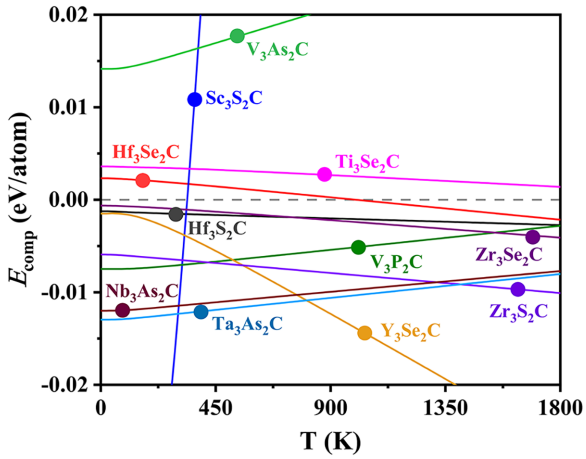

FIG. 7. E_{comp} values of M_3A_2X phases as a function of temperature.

formation energy of Sc_3S_2C rises rapidly with the increase of temperature and turns from negative to positive at approximately 340 K, meaning that the phase becomes unstable. The variation trend of the E_{comp} of Sc_3S_2C is strange and different with other M_3A_2X phases. To identify the reason, we have plotted the curves of free energy versus temperature for all four stable M_3A_2X phases with A = S and their corresponding competing phases (see Fig. S.2 [64]). It can be found that the free energy trends of all compounds are quite similar, and only the free energy of Sc_5S_4C decreases rapidly with the increase of temperature. Therefore, it can be concluded that the rapid increase in E_{comp} for Sc_3S_2C is caused by the rapid decrease in the free energy of the competing phase Sc_5S_4C.

In brief, we obtained 11 stable and one high-temperature stable M_3A_2X phases in thermodynamics from 240 M_3A_2X candidates. The crystal structure information (crystal system, space group, lattice parameters, and atomic coordinates) of these 12 stable M_3A_2X phases is listed in Table S.4 [64]. Among them, nine phases are newly discovered and have never been reported before. In particular, crystal structure [trigonal, $P\bar{3}m1$, Fig. 1(e)] of Sc_3S_2C, Y_3S_2C, and Y_3Se_2C are novel and different from that [hexagonal, $P6_3/mmc$, Fig. 1(d)] of synthesized M_3A_2X phases [31].

It is particularly noteworthy that thermodynamically unstable M_3A_2X phases with positive E_{comp} values in Table S.3 [64] can also be experimentally synthesized. Approximately 20% of the compounds in the Inorganic Crystal Structure Database [74] exhibit formation energies exceeding 0.036 eV/atom. Some top-down approaches (such as molten salt synthesis) [13] or thin film processing [15] can obtain metastable or far from thermodynamically stable *MAX* phases [1,3,4].

2. Dynamic stability

Dynamic stability of a phase refers to the ability of its crystal structure against small atomic displacements and can be judged from no imaginary frequencies in its phonon dispersion spectrum. The calculated phonon dispersion spectra of all 12 thermodynamically stable M_3A_2X phases are presented in Fig. S.3 [64]. Nb_3As_2C and Y_3S_2C, as representatives of the

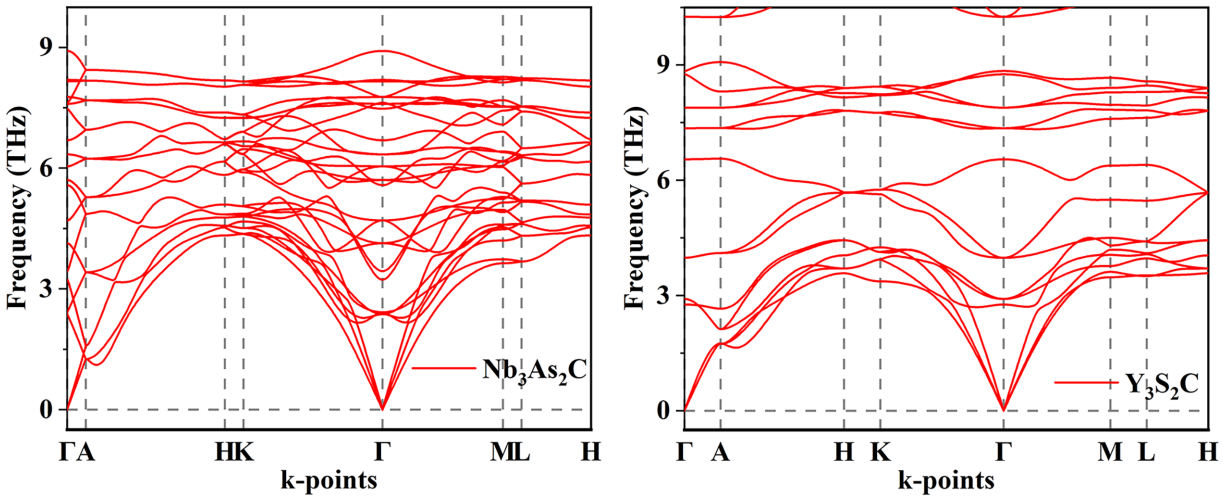

FIG. 8. Phonon dispersion spectra of Nb_3As_2C and Y_3S_2C phases.

No. 4 and 51 configurations, respectively, have their phonon dispersion spectra shown in Fig. 8. No imaginary frequencies were observed within the whole phonon dispersion ranges of the 12 M_3A_2X phases, indicating dynamic stability.

3. Mechanical stability

Mechanical stability, which refers to the ability of a structure to resist deformations or distortions in terms of strain, can be evaluated by checking whether its elastic constants meet the Born stability conditions. For hexagonal system (No. 4 configuration, $P6_3/mmc$), its five independent elastic constants (C_{11}, C_{12}, C_{13}, C_{33}, C_{44}) should meet the stability criterion: $C_{11} > 0$, $C_{44} > 0$, $C_{11} > C_{12}$, $(C_{11} + C_{12})C_{33} - 2C_{13}^2 > 0$. For a trigonal system (No. 51 configuration, $P\bar{3}m1$), its six independent elastic constants (C_{11}, C_{12}, C_{13}, C_{14}, C_{33}, C_{44}) should meet the stability criterion: $C_{11} > 0$, $C_{44} > 0$, $C_{11} > C_{12}$, $(C_{11} + C_{12})C_{33} - 2C_{13}^2 > 0$, $(C_{11} - C_{12})C_{44} - 2C_{14}^2 > 0$. Elastic constants of the 12 thermodynamically stable M_3A_2X phases are given in Table II. The elastic constants of all the 12 M_3A_2X phases satisfy the above criteria, indicating their mechanical stabilities.

D. Electronic properties

Band structures and density of states (DOS) of the 12 thermodynamically stable M_3A_2X phases were calculated to evaluate their electronic properties, as depicted in Fig. S.4 and Fig. S.5 [64]. Nb_3As_2C and Y_3S_2C, as representatives of the No. 4 and 51 configurations, respectively, have their DOS curves shown in Fig. 9. All 12 M_3A_2X phases exhibit metallic conductivity, which mainly comes from the *d* electron of *M* atoms. From the local DOS presented in Fig. 9, the bonding states of *M*-*A* and *M*-*C* can be discerned through the hybridization between the *d* orbitals of *M* atoms and the *p* orbitals of A atoms or the *p* orbitals of C atoms.

For a class of materials with similar crystal structures, the DOS at Fermi level can be used to quantitatively compare their relative electrical conductivities [71]. Figure 10 illustrates the DOS values at the Fermi level of the 12 stable M_3A_2X phases in comparison with their corresponding M_2AX phases. Previous work [71] has indicated that the DOS at Fermi level is reasonably correlated with the total valence electron number per volume. However, this correlation in M_3A_2X and M_2AX is not clearly discernible from Fig. 10. Perhaps this is due to the relatively small number of phases in the calculation of DOS. We observed that the DOS values at Fermi level for the

TABLE II. Elastic constants of the 12 thermodynamically stable M_3A_2X phases (GPa).

Phase	Crystal system	C_{11}	C_{12}	C_{13}	C_{14}	C_{33}	C_{44}	C_{66}
Sc_3S_2C	Trigonal	219.98	59.26	63.66	−15.93	191.68	85.77	80.36
Y_3S_2C	Trigonal	186.36	51.55	60.43	−18.87	159.66	77.11	67.40
Y_3Se_2C	Trigonal	160.48	47.70	55.54	−18.27	143.61	66.92	56.39
Zr_3S_2C	Hexagonal	264.92	88.11	98.49	–	293.62	132.47	88.41
Zr_3Se_2C	Hexagonal	234.50	76.85	91.56	–	256.14	121.44	78.82
Hf_3S_2C	Hexagonal	294.80	91.51	108.26	–	310.00	145.81	101.65
Hf_3Se_2C	Hexagonal	260.67	79.40	98.74	–	268.43	130.13	90.63
V_3P_2C	Hexagonal	339.52	107.44	158.73	–	398.52	207.19	116.04
Nb_3As_2C	Hexagonal	295.90	101.42	141.37	–	341.48	168.01	97.24
Nb_3P_2C	Hexagonal	332.44	109.95	153.93	–	395.49	186.79	111.24
Ta_3As_2C	Hexagonal	316.97	108.25	153.46	–	368.69	179.84	104.36
Ta_3P_2C	Hexagonal	355.57	118.79	169.15	–	424.50	203.27	118.39

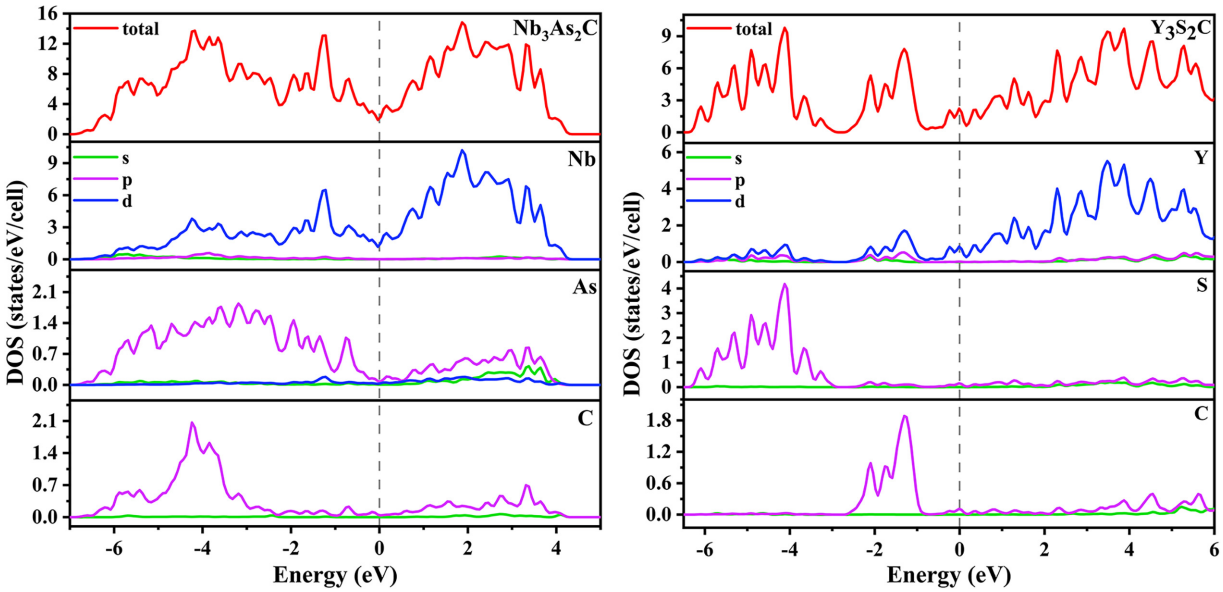

FIG. 9. Local density of states (LDOS) of Nb_3As_2C and Y_3S_2C phases.

majority of M_3A_2X phases (nine out of 12) are higher than those of their corresponding M_2AX phases. This implies that M_3A_2X phases have generally better electrical conductivity than M_2AX phases. Among the stable M_3A_2X phases, V_3P_2C has the best electrical conductivity.

E. Mechanical properties

Micromechanical properties, such as bulk and shear moduli, are of great significance because they play an important role in macromechanical properties, including lubrication, friction, and machinability. Experimental investigation into the micromechanical properties of the *MAX* phase has been obstructed by the difficulties in obtaining pure samples. The micromechanical properties of polycrystalline samples can be calculated from the corresponding elastic constants according to so-called Voigt-Reuss-Hill approximations. The Voigt and Reuss values represent the upper and lower limits of the elastic constants of polycrystalline, respectively. The Hill value is the average of the Voigt and Reuss values, and thus can be thought of as practical estimates.

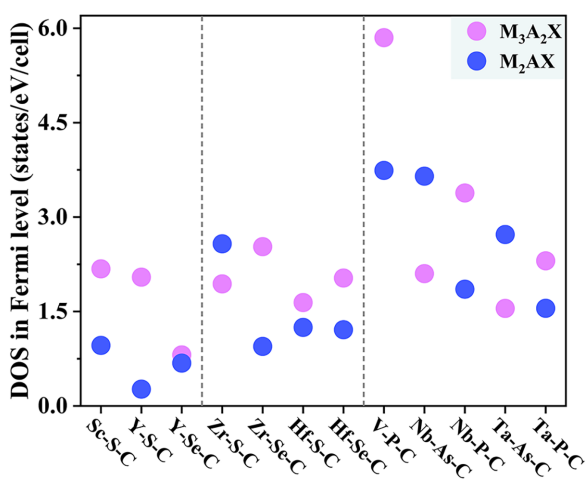

FIG. 10. DOS values at Fermi level of the 12 stable M_3A_2X phases in comparison with their corresponding M_2AX phases.

The bulk modulus (B) serves as a metric for the volume compressibility of a material, and the shear modulus (G) measures the average shearability of the material, which can be obtained as follows:

$$B_V = [(C_{11} + C_{22} + C_{33}) + 2(C_{12} + C_{13} + C_{23})]/9,$$

$$G_V = [(C_{11} + C_{22} + C_{33}) - (C_{12} + C_{13} + C_{23}) + 3(C_{44} + C_{55} + C_{66})]/15,$$

$$B_R = 1/[(S_{11} + S_{22} + S_{33}) + 2(S_{12} + S_{13} + S_{23})],$$

$$G_R = 15/[4(S_{11} + S_{22} + S_{33}) - 4(S_{12} + S_{13} + S_{23}) + 3(S_{44} + S_{55} + S_{66})],$$

$$B = B_H = (B_V + B_R)/2, \quad G = G_H = (G_V + G_R)/2,$$

where S_{ij} is the elastic compliance, and the subscripts V, R, and H denote the Voigt, Reuss, and Hill moduli, respectively. The Young's modulus (E), Poisson's ratio (v), and Pugh's ratio (k) can be calculated using the following equations:

$$E = 9BG/(3B + G), \; v = (3B - 2G)/(6B + 2G), \; k = G/B.$$

The Vickers hardness (H_V) is taken as the average value of the hardness values (see Table S.5 [64]) calculated by the following four formulas [75–78]:

$$H_{Chen} = 2(k^2G)^{0.585} - 3, \; H_{Tian} = 0.92k^{1.137}G^{0.708}, \; H_{Miao} = (1-2v)E/[6(1+v)], \; H_{Jiang} = G/6.78.$$

The data of micromechanical properties of the 12 stable M_3A_2X phases are presented in Table III. For greater intuitiveness, the B and G moduli are plotted in Figs. 11(a) and 11(b). The B (G) value spreads in a wide range and varies from 86.9 (57.9) GPa in Y_3Se_2C to 225.3 (144.2) GPa in Ta_3P_2C, indicating broad potential applications in various areas. The B value of Ta_3P_2C is higher than those of four

TABLE III. Calculated bulk modulus B (GPa), shear modulus G (GPa), Young's modulus E (GPa), Pugh's ratio k, Poisson's ratio υ, Vickers hardness H_V (GPa) of the 12 stable M_3A_2X phases in comparison with their corresponding M_2AX phases.

Phase	B	G	E	k	υ	H_V	Phase	B	G	E	k	υ	H_V
Sc_3S_2C	111.5	79.7	193.2	0.72	0.21	13.9	Sc_2SC	125.7	91.0	219.9	0.72	0.21	15.7
Y_3S_2C	97.3	67.6	164.8	0.70	0.22	11.8	Y_2SC	104.0	71.9	175.3	0.69	0.22	12.3
Y_3Se_2C	86.9	57.9	142.0	0.67	0.23	9.9	Y_2SeC	97.3	67.1	163.6	0.69	0.22	11.6
Zr_3S_2C	154.5	104.6	256.0	0.68	0.22	16.7	Zr_2SC	164.2	113.1	275.8	0.69	0.22	18.1
Zr_3Se_2C	138.0	93.1	228.1	0.68	0.23	15.1	Zr_2SeC	151.7	103.4	252.9	0.68	0.22	16.7
Hf_3S_2C	168.2	116.0	283.0	0.69	0.22	18.5	Hf_2SC	177.1	125.7	304.9	0.71	0.21	20.4
Hf_3Se_2C	149.1	102.3	249.7	0.69	0.22	16.6	Hf_2SeC	162.3	114.5	278.0	0.71	0.21	18.8
V_3P_2C	211.9	142.5	349.2	0.67	0.23	21.6	V_2PC	232.1	149.0	368.2	0.64	0.24	21.5
Nb_3As_2C	187.5	118.0	292.7	0.63	0.24	17.4	Nb_2AsC	204.4	120.5	302.1	0.59	0.25	16.9
Nb_3P_2C	208.6	134.7	332.5	0.65	0.23	20.0	Nb_2PC	223.3	139.4	346.2	0.62	0.24	20.0
Ta_3As_2C	201.8	126.3	313.6	0.63	0.24	18.4	Ta_2AsC	219.1	128.8	323.0	0.59	0.25	17.9
Ta_3P_2C	225.3	144.2	356.4	0.64	0.24	21.0	Ta_2PC	240.3	148.4	369.2	0.62	0.24	21.1

synthesized M_3A_2X phases and close to the known maximum value (Ta_4AlC_3, 266 GPa) [34] of *MAX* phases. From Figs. 11(a) and 11(b), we noticed that the B and G values depend on M and A elements. As the M element ranges from Group IIIB to VB, the values of B and G gradually increase. For the A element from Group VA to VIA, the trends of B and G values are reversed. Our findings are consistent with the previous results about traditional *MAX* phases [70,79], in which elastic properties were found to be dependent on valence electrons of the constituent elements.

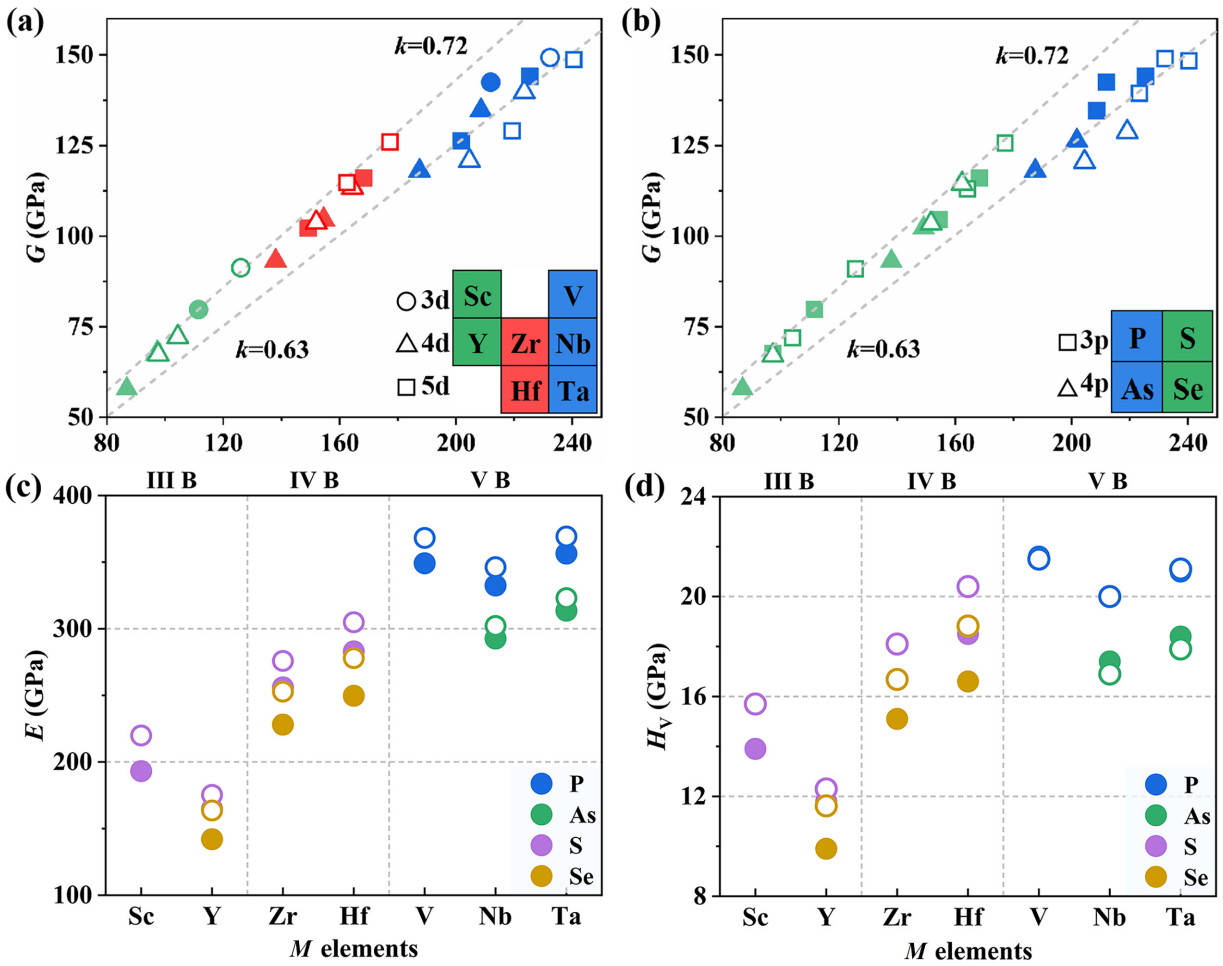

FIG. 11. (a), (b) Bulk modulus (B), shear modulus (G), (c) Young's modulus (E) and (d) Vickers hardness (H_V) of the 12 stable M_3A_2X phases in comparison with their corresponding M_2AX phases. The solid and empty symbols represent the M_3A_2X and M_2AX phases, respectively.

The Young's modulus (E) serves as a crucial indicator of a material's stiffness. Since E is calculated from B and G, it exhibits the same variation trend as B and G [seen from Fig. 11(c)]. The Vickers hardness [H_V shown in Fig. 11(d)] ranges from 9.9 to 21.6 GPa. The M_3A_2X phases with M in Group VB exhibit high hardness, in which, V_3P_2C has the highest hardness of 21.6 GPa. Poisson's ratio (υ) provides the overall bonding characteristics of a material. Since the M and A elements in the 12 stable M_3A_2X phases are narrowly distributed in the periodic table, the bond characteristics of these phases are similar. As a result, their Poisson's ratio values are close and fall within a narrow range from 0.21 to 0.24. Pugh's ratio (k) can identify the brittleness and ductility of a material. A higher Pugh's ratio (>0.57) indicates that the material is more likely to be brittle, while a lower ratio (<0.57) suggests greater ductility. The k of the 12 M_3A_2X phases falls within the narrow range of 0.63–0.72 [seen from Figs. 11(a) and 11(b)], indicating that all of them are brittle.

We calculated the micromechanical properties of traditional M_2AX phases and compared their results with those of the M_3A_2X phases, as shown in Table III and Fig. 11. In Figs. 11(a) and 11(b), the B and G values of M_3A_2X are located in the lower-left corner of the corresponding M_2AX, indicating that the B and G of M_3A_2X are weaker than those of M_2AX. Correspondingly, all E values and most H_V values of M_3A_2X are lower than those of M_2AX. Only the H_V values of M_3A_2X with M in Group VB are slightly higher. Overall, the mechanical properties of the M_3A_2X phases are slightly weaker than those of the M_2AX phases.

Theoretical mechanical properties of a material depend on its crystal structure and the constituent chemical bonds. Considering that M_3A_2X and M_2AX have similar crystal structures, bond strength plays a crucial role in determining the mechanical properties. The COHP analysis was carried out to compare the bond strength in M_3A_2X and M_2AX. The bonding strength can be determined quantitatively by integrating the bonding states of the -COHP curves up to the Fermi level. A larger -ICOHP value implies a stronger bond.

Figure 12(a) illustrates the -ICOHP values of the M-C and M-A bonds of the 12 stable M_3A_2X phases in comparison with their corresponding M_2AX phases. It should be noted that there are two types of M-A bonds in M_3A_2X: $M1$-A and $M2$-A (see Fig. 1). The -ICOHP values of M-A and M-C bonds in M_3A_2X are higher when M is in Group VB than in Group IIIB or IVB, suggesting stronger bonds in the former case. This finding is highly consistent with the previous results of mechanical properties. Compared with the M-A bonds in M_2AX, the $M1$-A bonds in the corresponding M_3A_2X become stronger, while the $M2$-A bonds are weaker. Meanwhile, the M-C bonds in M_3A_2X are weaker than those in the corresponding M_2AX phase. Overall, the atomic interactions in M_3A_2X are slightly weaker than those in the corresponding M_2AX. As a result, M_3A_2X has slightly inferior mechanical properties to M_2AX.

The M-C and M-A bond lengths in both M_3A_2X and M_2AX are presented in Fig. 12(b). Upon careful observation, it can be found that, compared with the M_2AX phase, the variation trend of the bond length in M_3A_2X is opposite to that of the bond strength. As shown in Fig. 12(c), there is basically an inverse relationship between the bond length and the bond strength of the MAX phases. This indicates that for the same type of chemical bonds, bond length, to some extent, can reflect bond strength, which is also in line with general knowledge.

F. Magnetic properties

To check magnetic properties of the 12 stable M_3A_2X phases, we calculated their spin-resolved DOS (see Fig. S.6 [64]). The spin-up and spin-down states for each stable M_3A_2X phase are completely symmetric and the magnetic moments of all the 12 M_3A_2X are $0\,\mu_B$, indicating their nonmagnetic properties. Mn_2GaC is the first experimentally discovered MAX phase with magnetism [80]. We also calculated the spin-resolved DOS of Mn_2GaC (see Fig. S.7 [64]). Its spin-up and spin-down states are asymmetric, displaying ferromagnetic state. The total and Mn magnetic moments are calculated to be 6.69 and $1.78\,\mu_B$, which is consistent with experiment result [80]. The discovered magnetic MAX phases contained either Mn or Cr [81]. However, among the 12 stable M_3A_2X phases we predicted, none include the above two elements. Therefore, it is reasonable that they do not exhibit magnetism.

G. Exfoliation of the M_3A_2X phases to form 2D MXenes

As previously mentioned, MAX phases can be exfoliated into 2D MXenes. In addition to static exfoliation energy [40,82–84], bond strengths represented by force constant [40,82,84] or COHP [82,84] have been used to explore the exfoliation potential of MAX phases to form 2D MXenes. In this section, we used the above calculated COHP results to investigate the exfoliation possibility of the 12 stable M_3A_2X phases by physical exfoliation methods.

As can be seen in Fig. 12(a), the M-C bonds are significantly stronger than the M-A bonds, which is the reason 2D MXenes were prepared by cleaving the M-A bonds in MAX phases. Weak M-A bonds are the primary condition for exfoliating MAX phases. However, this condition alone is inadequate. It is also required that the M-C bonds should be relatively strong. Otherwise, the MAX phases will completely collapse to form other bulk materials during exfoliation and will not be able to retain the 2D MXene sheets. Thus we use the -ICOHP ratio of M-A bond to M-C bond to represent the ease of exfoliation of MAX phases in forming 2D MXenes. Lower -ICOHP ratio values indicate a higher possibility of exfoliation.

Figure 12(d) illustrates the -ICOHP ratios of M-A bonds to M-C bonds of the 12 stable M_3A_2X phases and their corresponding M_2AX phases. The -ICOHP ratios of all M_3A_2X and M_2AX are < 1, meaning that M-A bonds are weaker than M-C bonds. Since M-A bonds in M_2AX are weaker than $M1$-A bonds but stronger than $M2$-A bonds in M_3A_2X, the -ICOHP ratios of M-A to M-C in M_2AX are smaller than those of $M1$-A to M-C in M_3A_2X, yet larger than those of $M2$-A to M-C bonds in M_3A_2X. During the exfoliation process, the $M2$-A bonds in M_3A_2X are preferentially cleaved. Therefore, M_3A_2X can be more easily exfoliated into 2D MXenes than corresponding M_2AX. The Zr_3Se_2C, Zr_3S_2C, and Sc_3S_2C phases exhibit the

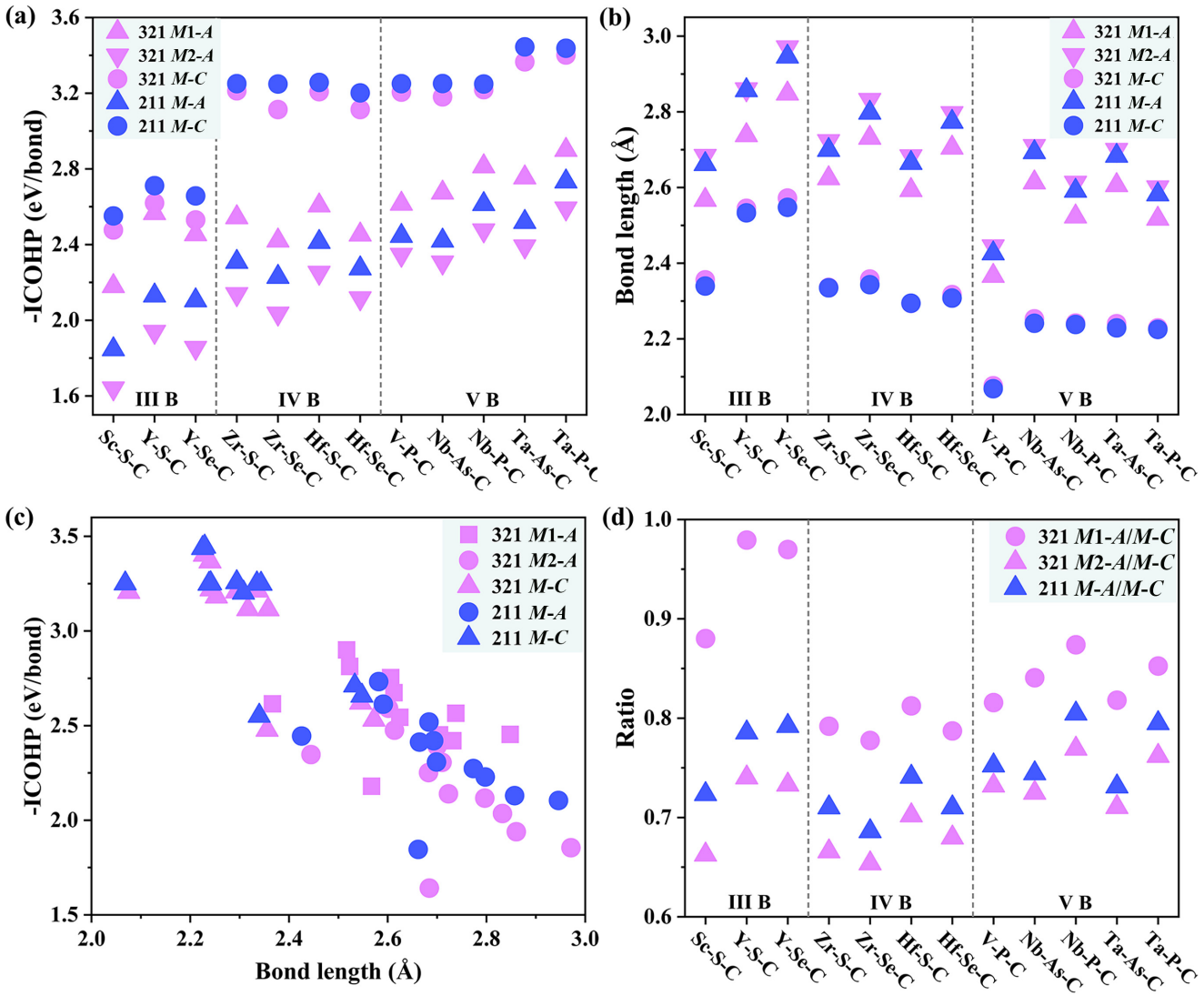

FIG. 12. (a) Bond -ICOHP values, (b) bond lengths, (c) bond -ICOHP values as a function of bond lengths, and (d) bond -ICOHP ratio of *M-A* to *M-C* of the 12 stable M_3A_2X phases and their corresponding M_2AX phases. The 321 and 211 represent M_3A_2X phase and M_2AX phase, respectively.

lowest -ICOHP ratios of *M2-A* to *M-C*. Thus, they are expected to be the most readily exfoliated. Notably, since 2D Zr- and Sc-based MXenes have not been successfully synthesized so far, the predicted stability and high exfoliation potential of the Zr_3Se_2C, Zr_3S_2C, and Sc_3S_2C phases hold even greater practical significance.

IV. CONCLUSIONS

In this research, a high-throughput computational method was utilized to conduct a comprehensive investigation of the M_3A_2X phases. Through three rounds of stability assessment, 12 stable M_3A_2X phases were screened out from 240 possible compositions. Notably, nine phases are newly discovered and have never been reported before. Three (Sc_3S_2C, Y_3S_2C, and Y_3Se_2C) of the stable M_3A_2X phases possess novel structures distinct from those of synthesized M_3A_2X phases, which validates the necessity of considering various structures during identifying the lowest-energy structure. Our recommendation to experimental researchers is that Y_3S_2C and Ta_3As_2C are more readily synthesizable among them. Since some M_3A_2X phases are stable only at high temperatures while some become unstable at high temperatures, the selection of temperature is crucial in experimental synthesis. Because binary *M-A* and M-X phases are the main competitors to the stability of M_3A_2X, it is necessary to avoid using those as raw materials during the synthesis of M_3A_2X.

Because the proportion of *M* atoms in M_3A_2X is higher than that in M_2AX, M_3A_2X phases generally exhibit better electrical conductivity than their corresponding classic M_2AX phases. Among the stable M_3A_2X phases, V_3P_2C possesses the best electrical conductivity. Due to having weaker atomic interactions in M_3A_2X than M_2AX, M_3A_2X phases demonstrate slightly inferior mechanical properties to their corresponding M_2AX phases. M_3A_2X phases possess different electrical and mechanical properties from those of known *MAX* phases, enabling it to identify suitable application areas.

We also investigate the exfoliation possibility of the 12 stable M_3A_2X phases through analyzing bond strength based on COHP value. The results show that M_3A_2X can be more easily exfoliated into 2D MXenes than corresponding M_2AX. Zr_3Se_2C, Zr_3S_2C, and Sc_3S_2C are expected to be the most readily exfoliated, which holds even greater practical significance for the development of new Zr-and Sc-based MXenes.

ACKNOWLEDGMENTS

This work was supported by the National Natural Science Foundation of China (Grants No. 52372284, No. 52275187, No. 52202364, and No. 52102017).

DATA AVAILABILITY

The data supporting this study's findings are available within the article.

[1] M. W. Barsoum, The $M_{N+1}AX_N$ phases: A new class of solids: Thermodynamically stable nanolaminates, Prog. Solid State Chem. **28**, 201 (2000).

[2] A. G. Zhou, Y. Liu, S. B. Li, X. H. Wang, G. B. Ying, Q. X. Xia, and P. G. Zhang, From structural ceramics to 2D materials with multi-applications: A review on the development from MAX phases to MXenes, J. Adv. Ceram. **10**, 1194 (2021).

[3] L. Fu and W. Xia, MAX phases as nanolaminate materials: Chemical composition, microstructure, synthesis, properties, and applications, Adv. Eng. Mater. **23**, 2001191 (2021).

[4] M. Dahlqvist, M. W. Barsoum, and J. Rosen, MAX phases—Past, present, and future, Mater. Today **72**, 1 (2024).

[5] H. Rohde and H. Kudielka, Strukturuntersuchungen an Carbosulfiden von Titan und Zirkon, Z. Kristallogr.-Cryst. Mater. **114**, 447 (1960).

[6] M. W. Barsoum and T. Elraghy, Synthesis and characterization of a remarkable ceramic: Ti_3SiC_2, J. Am. Ceram. Soc. **79**, 1953 (1996).

[7] M. W. Barsoum, D. Brodkin, and T. El-Raghy, Layered machinable ceramics for high temperature applications, Scripta Mater. **36**, 535 (1997).

[8] M. Naguib, M. Kurtoglu, V. Presser, J. Lu, J. J. Niu, M. Heon, L. Hultman, Y. Gogotsi, and M. W. Barsoum, Two-dimensional nanocrystals produced by exfoliation of Ti_3AlC_2, Adv. Mater. **23**, 4248 (2011).

[9] M. Li, Y.-B. Li, K. Luo, J. Lu, E. Per, P. Per, R. Johanna, H. Lars, S.-Y. Du, Z.-R. Huang, and Q. Huang, Synthesis of novel *MAX* phase Ti_3ZnC_2 via A-site-element-substitution approach, J. Inorg. Mater. **34**, 60 (2019).

[10] M. Li, J. Lu, K. Luo, Y. B. Li, K. K. Chang, K. Chen, J. Zhou, J. Rosen, L. Hultman, P. Eklund, P. O. A. Persson, S. Y. Du, Z. F. Chai, Z. R. Huang, and Q. Huang, Element replacement approach by reaction with Lewis acidic molten salts to synthesize nanolaminated MAX phases and MXenes, J. Am. Chem. Soc. **141**, 4730 (2019).

[11] H. M. Ding, Y. B. Li, J. Lu, K. Luo, K. Chen, M. Li, P. O. A. Persson, L. Hultman, P. Eklund, S. Y. Du, Z. R. Huang, Z. F. Chai, H. J. Wang, P. Huang, and Q. Huang, Synthesis of MAX phases Nb_2CuC and $Ti_2(Al_{0.1}Cu_{0.9})N$ by A-site replacement reaction in molten salts, Mater. Res. Lett. **7**, 510 (2019).

[12] Y. B. Li, S. R. Zhu, E. R. Wu, H. M. Ding, J. Lu, X. L. Mu, L. Chen, Y. M. Zhang, J. Palisaitis, K. Chen, M. Li, P. F. Yan, P. O. A. Persson, L. Hultman, P. Eklund, S. Y. Du, Y. B. Kuang, Z. F. Chai, and Q. Huang, Nanolaminated ternary transition metal carbide (MAX phase)-derived core–shell structure electrocatalysts for hydrogen evolution and oxygen evolution reactions in alkaline electrolytes, J. Phys. Chem. Lett. **14**, 481 (2023).

[13] H. M. Ding, Y. B. Li, M. Li, K. Chen, K. Liang, G. X. Chen, J. Lu, J. Palisaitis, P. O. A. Persson, P. Eklund, L. Hultman, S. Y. Du, Z. F. Chai, Y. Gogotsi, and Q. Huang, Chemical scissor–mediated structural editing of layered transition metal carbides, Science **379**, 1130 (2023).

[14] H. Fashandi, M. Dahlqvist, J. Lu, J. Palisaitis, S. I. Simak, I. A. Abrikosov, J. Rosen, L. Hultman, M. Andersson, A. Lloyd Spetz, and P. Eklund, Synthesis of Ti_3AuC_2, $Ti_3Au_2C_2$ and Ti_3IrC_2 by noble metal substitution reaction in Ti_3SiC_2 for high-temperature-stable Ohmic contacts to SiC, Nat. Mater. **16**, 814 (2017).

[15] H. Fashandi, C.-C. Lai, M. Dahlqvist, J. Lu, J. Rosen, L. Hultman, G. Greczynski, M. Andersson, A. Lloyd Spetz, and P. Eklund, Ti_2Au_2C and $Ti_3Au_2C_2$ formed by solid state reaction of gold with Ti_2AlC and Ti_3AlC_2, Chem. Commun. **53**, 9554 (2017).

[16] C. C. Lai, H. Fashandi, J. Lu, J. Palisaitis, P. O. A. Persson, L. Hultman, P. Eklund, and J. Rosen, Phase formation of nanolaminated Mo_2AuC and $Mo_2(Au_{1-x}Ga_x)_2C$ by a substitutional reaction within Au-capped Mo_2GaC and Mo_2Ga_2C thin films, Nanoscale **9**, 17681 (2017).

[17] C. C. Lai, Q. Z. Tao, H. Fashandi, U. Wiedwald, and J. Rosen, Magnetic properties and structural characterization of layered $(Cr_{0.5}Mn_{0.5})_2AuC$ synthesized by thermally induced substitutional reaction in $(Cr_{0.5}Mn_{0.5})_2GaC$, APL Mater. **6**, 026104 (2018).

[18] Q. Q. Zhang, Y. C. Zhou, X. Y. San, D. T. Wan, Y. W. Bao, Q. G. Feng, S. Grasso, and C. F. Hu, Thermal explosion synthesis of first Te-containing layered ternary Hf_2TeB MAX phase, J. Eur. Ceram. Soc. **43**, 173 (2023).

[19] K. Chen, X. J. Bai, X. L. Mu, P. F. Yan, N. X. Qiu, Y. B. Li, J. Zhou, Y. J. Song, Y. M. Zhang, S. Y. Du, Z. F. Chai, and Q. Huang, MAX phase Zr_2SeC and its thermal conduction behavior, J. Eur. Ceram. Soc. **41**, 4447 (2021).

[20] X. D. Wang, K. Chen, E. X. Wu, Y. M. Zhang, H. M. Ding, N. X. Qiu, Y. J. Song, S. Y. Du, Z. F. Chai, and Q. Huang, Synthesis and thermal expansion of chalcogenide MAX phase Hf_2SeC, J. Eur. Ceram. Soc. **42**, 2084 (2022).

[21] Q. Q. Zhang, Y. C. Zhou, X. Y. San, W. B. Li, Y. W. Bao, Q. G. Feng, S. Grasso, and C. F. Hu, Zr_2SeB and Hf_2SeB: Two new MAB phase compounds with the Cr_2AlC-type MAX phase (211 phase) crystal structures, J. Adv. Ceram. **11**, 1764 (2022).

[22] J. Luo, F. J. Zhang, B. Wen, Q. Q. Zhang, L. S. Chu, Y. C. Zhou, Q. G. Feng, and C. F. Hu, Theoretical prediction and experimental synthesis of Zr_3AC_2 (A = Cd, Sb) phases, Materials **17**, 1556 (2024).

[23] Q. Q. Zhang, J. Luo, B. Wen, Y. C. Zhou, L. S. Chu, Q. G. Feng, and C. F. Hu, Determination of new a-312 MAX phases of Zr_3InC_2 and Hf_3InC_2, J. Eur. Ceram. Soc. **43**, 7228 (2023).

[24] Q. Q. Zhang, B. Wen, J. Luo, Y. C. Zhou, X. Y. San, Y. W. Bao, L. S. Chu, Q. G. Feng, S. Grasso, and C. F. Hu, Synthesis of new lead-containing MAX phases of Zr_3PbC_2 and Hf_3PbC_2, J. Am. Ceram. Soc. **106**, 6390 (2023).

[25] Q. Q. Zhang, B. Wen, J. Luo, Y. C. Zhou, X. Y. San, Y. W. Bao, Q. G. Feng, S. Grasso, and C. F. Hu, Synthesis of new rare earth containing ternary laminar Sc_2PbC ceramic, J. Eur. Ceram. Soc. **43**, 1735 (2023).

[26] Q. Q. Zhang, J. Luo, B. Wen, Y. C. Zhou, X. Y. San, H. Chen, Q. G. Feng, and C. F. Hu, Synthesis of new rare earth containing MAX phases Sc_2AC (A = Ga, In) by spark plasma sintering, J. Am. Ceram. Soc. **107**, 3644 (2024).

[27] T. Rackl, L. Eisenburger, R. Niklaus, and D. Johrendt, Syntheses and physical properties of the MAX phase boride Nb_2SB and the solid solutions $Nb_2SB_xC_{1-x}(x = 0–1)$, Phys. Rev. Mater. **3**, 054001 (2019).

[28] T. Rackl and D. Johrendt, The MAX phase borides Zr_2SB and Hf_2SB, Solid State Sci. **106**, 106316 (2020).

[29] Q. Q. Zhang, S. Fu, D. T. Wan, Y. W. Bao, Q. G. Feng, S. Grasso, and C. F. Hu, Rapidly synthesizing Hf_2SB ceramics by thermal explosion, J. Eur. Ceram. Soc. **42**, 3780 (2022).

[30] Q. Q. Zhang, S. Fu, D. T. Wan, Y. W. Bao, Q. G. Feng, S. Grasso, and C. F. Hu, Synthesis and property characterization of ternary laminar Zr_2SB ceramic, J. Adv. Ceram. **11**, 825 (2022).

[31] H. X. Chen, D. L. Yang, Q. H. Zhang, S. F. Jin, L. W. Guo, J. Deng, X. D. Li, and X. L. Chen, A series of MAX phases with MA-triangular-prism bilayers and elastic properties, Angew. Chem. Int. Ed. **58**, 4576 (2019).

[32] H. X. Chen, S. Li, J. Deng, Z. L. Zhang, J. N. Huang, F. Chang, L. Huang, S. X. Du, and P. Q. Dai, Synthesis, formation mechanism, and intrinsic physical properties of several As/P-containing MAX phases, J. Mater. Sci. Technol. **133**, 23 (2023).

[33] H. X. Chen, Z. L. Zhang, J. Deng, Z. J. Lin, C. F. Hong, S. X. Du, and P. Q. Dai, Observation of low thermal expansion behavior and weak thermal anisotropy in M_3A_2C phases, J. Mater. Sci. Technol. **154**, 210 (2023).

[34] B. Manoun, S. K. Saxena, T. El-Raghy, and M. W. Barsoum, High-pressure x-ray diffraction study of Ta_4AlC_3, Appl. Phys. Lett. **88**, 201902 (2006).

[35] M. A. Hadi, M. A. Rayhan, S. H. Naqib, A. Chroneos, and A. K. M. A. Islam, Structural, elastic, thermal and lattice dynamic properties of new 321 MAX phases, Comput. Mater. Sci. **170**, 109144 (2019).

[36] S. Curtarolo, G. L. W. Hart, M. B. Nardelli, N. Mingo, S. Sanvito, and O. Levy, The high-throughput highway to computational materials design, Nat. Mater. **12**, 191 (2013).

[37] V. J. Keast, S. Harris, and D. K. Smith, Prediction of the stability of the $M_{n+1}AX_n$ phases from first principles, Phys. Rev. B **80**, 214113 (2009).

[38] M. Dahlqvist, B. Alling, and J. Rosen, Stability trends of MAX phases from first principles, Phys. Rev. B **81**, 220102(R) (2010).

[39] M. Ashton, R. G. Hennig, S. R. Broderick, K. Rajan, and S. B. Sinnott, Computational discovery of stable M_2AX phases, Phys. Rev. B **94**, 054116 (2016).

[40] R. Khaledialidusti, M. Khazaei, S. Khazaei, and K. Ohno, High-throughput computational discovery of ternary-layered MAX phases and prediction of their exfoliation for formation of 2D MXenes, Nanoscale **13**, 7294 (2021).

[41] M. Dahlqvist and J. Rosen, Predictive theoretical screening of phase stability for chemical order and disorder in quaternary 312 and 413 MAX phases, Nanoscale **12**, 785 (2020).

[42] A. Poulou, T. A. Mellan, and M. W. Finnis, Stability of Zr-Al-C and Ti-Al-C MAX phases: A theoretical study, Phys. Rev. Mater. **5**, 033608 (2021).

[43] M. Dahlqvist and J. Rosen, The rise of MAX phase alloys—Large-scale theoretical screening for the prediction of chemical order and disorder, Nanoscale **14**, 10958 (2022).

[44] D. Ohmer, G. Qiang, I. Opahle, H. K. Singh, and H. B. Zhang, High-throughput design of 211-M_2AX compounds, Phys. Rev. Mater. **3**, 053803 (2019).

[45] P. Hohenberg and W. Kohn, Inhomogeneous electron gas, Phys. Rev. **136**, B864 (1964).

[46] W. Kohn and L. J. Sham, Self-consistent equations including exchange and correlation effects, Phys. Rev. **140**, A1133 (1965).

[47] G. Kresse and J. Furthmüller, Efficient iterative schemes for *ab initio* total-energy calculations using a plane-wave basis set, Phys. Rev. B **54**, 11169 (1996).

[48] J. P. Perdew, J. A. Chevary, S. H. Vosko, K. A. Jackson, M. R. Pederson, D. J. Singh, and C. Fiolhais, Atoms, molecules, solids, and surfaces: Applications of the generalized gradient approximation for exchange and correlation, Phys. Rev. B **46**, 6671 (1992).

[49] J. P. Perdew, K. Burke, and M. Ernzerhof, Generalized gradient approximation made simple, Phys. Rev. Lett. **77**, 3865 (1996).

[50] H. J. Monkhorst and J. D. Pack, Special points for Brillouin-zone integrations, Phys. Rev. B **13**, 5188 (1976).

[51] A. Togo, L. Chaput, T. Tadano, and I. Tanaka, Implementation strategies in phonopy and phono3py, J. Phys.: Condens. Matter **35**, 353001 (2023).

[52] A. Togo, First-principles phonon calculations with phonopy and phono3py, J. Phys. Soc. Jpn. **92**, 012001 (2023).

[53] Y. Le Page and P. Saxe, Symmetry-general least-squares extraction of elastic data for strained materials from *ab initio* calculations of stress, Phys. Rev. B **65**, 104104 (2002).

[54] S. Maintz, V. L. Deringer, A. L. Tchougréeff, and R. Dronskowski, LOBSTER: A tool to extract chemical bonding from plane-wave based DFT, J. Comput. Chem. **37**, 1030 (2016).

[55] A. Jain, S. P. Ong, G. Hautier, W. Chen, W. D. Richards, S. Dacek, S. Cholia, D. Gunter, D. Skinner, G. Ceder, and K. A. Persson, Commentary: The materials project: A materials genome approach to accelerating materials innovation, APL Mater. **1**, 011002 (2013).

[56] J. E. Saal, S. Kirklin, M. Aykol, B. Meredig, and C. Wolverton, Materials design and discovery with high-throughput density functional theory: The open quantum materials database (OQMD), JOM **65**, 1501 (2013).

[57] S. Kirklin, J. E. Saal, B. Meredig, A. Thompson, J. W. Doak, M. Aykol, S. Ruehl, and C. Wolverton, The Open Quantum Materials Database (OQMD): Assessing the accuracy of DFT formation energies, npj Comput. Mater. **1**, 15010 (2015).

[58] Y. B. Li, M. Li, J. Lu, B. K. Ma, and Q. Huang, Single-atom-thick active layers realized in nanolaminated $Ti_3(Al_xCu_{1-x})C_2$ and its artificial enzyme behavior, ACS Nano **13**, 9198 (2019).

[59] J. Etzkorn, M. Ade, D. Kotzott, M. Kleczek, and H. Hillebrecht, Ti_2GaC, Ti_4GaC_3 and Cr_2GaC—Synthesis, crystal growth and structure analysis of Ga-containing MAX-phases $M_{n+1}GaC_n$ with M = Ti, Cr and $n = 1, 3$, J. Solid State Chem. **182**, 995 (2009).

[60] J. Y. Wang, J. M. Wang, Y. C. Zhou, Z. J. Lin, and C. F. Hu, Ab initio study of polymorphism in layered ternary carbide M_4AlC_3 (M = V, Nb and Ta), Scripta Mater. **58**, 1043 (2008).

[61] J. J. Niu, H. B. Zhang, Y. Wu, C. F. Hu, and X. Wu, Pressure-induced reversible phase transition on Mo_2Ga_2C, J. Appl. Phys. **124**, 085903 (2018).

[62] C. C. Lai, R. Meshkian, M. Dahlqvist, J. Lu, L. A. Naslund, O. Rivin, E. N. Caspi, O. Ozeri, L. Hultman, P. Eklund, M. W. Barsoum, and J. Rosen, Structural and chemical determination of the new nanolaminated carbide Mo_2Ga_2C from first principles and materials analysis, Acta Mater. **99**, 157 (2015).

[63] H. C. Wang, J. N. Wang, X. F. Shi, Y. P. Wang, and B. Y. Tang, Possible new metastable Mo_2Ga_2C and its phase transition under pressure: A density functional prediction, J. Mater. Sci. **51**, 8542 (2016).

[64] See Supplemental Material at http://link.aps.org/supplemental/10.1103/stpc-qkpy for five tables (structural information, energy, the most stable competing phase, and Vickers hardness) and seven figures (structural model, phonon spectra, band structure, and density of state).

[65] M. Dahlqvist, B. Alling, I. A. Abrikosov, and J. Rosen, Phase stability of Ti_2AlC upon oxygen incorporation: A first-principles investigation, Phys. Rev. B **81**, 024111 (2010).

[66] A. S. Ingason, A. Mockute, M. Dahlqvist, F. Magnus, S. Olafsson, U. B. Arnalds, B. Alling, I. A. Abrikosov, B. Hjörvarsson, P. O. A. Persson, and J. Rosen, Magnetic self-organized atomic laminate from first principles and thin film synthesis, Phys. Rev. Lett. **110**, 195502 (2013).

[67] P. Eklund, M. Dahlqvist, O. Tengstrand, L. Hultman, J. Lu, N. Nedfors, U. Jansson, and J. Rosen, Discovery of the ternary nanolaminated compound by a systematic theoretical-experimental approach, Phys. Rev. Lett. **109**, 035502 (2012).

[68] A. Mockute, M. Dahlqvist, J. Emmerlich, L. Hultman, J. M. Schneider, P. O. A. Persson, and J. Rosen, Synthesis and *ab initio* calculations of nanolaminated $(Cr, Mn)_2AlC$ compounds, Phys. Rev. B **87**, 094113 (2013).

[69] Y. M. Zhang, Y. J. Xu, Q. Huang, S. Y. Du, M. Li, Y. B. Li, Z. Y. Mao, and Q. Han, Structure maps for MAX phases formability revisited, Ceram. Int. **50**, 2855 (2024).

[70] M. Khazaei, M. Arai, T. Sasaki, M. Estili, and Y. Sakka, Trends in electronic structures and structural properties of MAX phases: A first-principles study on M_2AlC (M = Sc, Ti, Cr, Zr, Nb, Mo, Hf, or Ta), M_2AlN, and hypothetical M_2AlB phases, J. Phys.: Condens. Matter **26**, 505503 (2014).

[71] S. Aryal, R. Sakidja, M. W. Barsoum, and W.-Y. Ching, A genomic approach to the stability, elastic, and electronic properties of the MAX phases, Phys. Status Solidi B **251**, 1480 (2014).

[72] C. J. Bartel, A. W. Weimer, S. Lany, C. B. Musgrave, and A. M. Holder, The role of decomposition reactions in assessing first-principles predictions of solid stability, npj Comput. Mater. **5**, 4 (2019).

[73] K. J. Bachmann, F. S. L. Hsu, F. A. Thiel, and H. M. Kasper, Debye temperature and standard entropies and enthalpies of compound semiconductors of the type I-III-VI2, J. Electron. Mater. **6**, 431 (1977).

[74] G. Bergerhoff, R. Hundt, R. Sievers, and I. Brown, The inorganic crystal structure data base, J. Chem. Inf. Comput. Sci. **23**, 66 (1983).

[75] X. Q. Chen, H. Y. Niu, D. Z. Li, and Y. Y. Li, Modeling hardness of polycrystalline materials and bulk metallic glasses, Intermetallics **19**, 1275 (2011).

[76] Y. Tian, B. Xu, and Z. Zhao, Microscopic theory of hardness and design of novel superhard crystals, Int. J. Refract. Met. Hard Mater. **33**, 93 (2012).

[77] N. Miao, B. Sa, J. Zhou, and Z. Sun, Theoretical investigation on the transition-metal borides with Ta_3B_4-type structure: A class of hard and refractory materials, Comput. Mater. Sci. **50**, 1559 (2011).

[78] X. Jiang, J. Zhao, and X. Jiang, Correlation between hardness and elastic moduli of the covalent crystals, Comput. Mater. Sci. **50**, 2287 (2011).

[79] M. F. Cover, O. Warschkow, M. M. M. Bilek, and D. R. McKenzie, A comprehensive survey of M_2AX phase elastic properties, J. Phys.: Condens. Matter **21**, 305403 (2009).

[80] A. S. Ingason, A. Petruhins, M. Dahlqvist, F. Magnus, A. Mockute, B. Alling, L. Hultman, I. A. Abrikosov, P. O. A. Persson, and J. Rosen, A nanolaminated magnetic phase: Mn_2GaC, Mater. Res. Lett. **2**, 89 (2014).

[81] A. S. Ingason, M. Dahlqvist, and J. Rosen, Magnetic MAX phases from theory and experiments; A review, J. Phys.: Condens. Matter **28**, 433003 (2016).

[82] J. Zhou, M. Dahlqvist, J. Bjork, and J. Rosen, Atomic scale design of MXenes and their parent materials—From theoretical and experimental perspectives, Chem. Rev. **123**, 13291 (2023).

[83] M. Khazaei, M. Arai, T. Sasaki, M. Estili, and Y. Sakka, The effect of the interlayer element on the exfoliation of layered Mo_2AC (A = Al, Si, P, Ga, Ge, As or In) MAX phases into two-dimensional Mo_2C nanosheets, Sci. Technol. Adv. Mater. **15**, 014208 (2014).

[84] M. Khazaei, A. Ranjbar, K. Esfarjani, D. Bogdanovski, R. Dronskowski, and S. Yunoki, Insights into exfoliation possibility of MAX phases to MXenes, Phys. Chem. Chem. Phys. **20**, 8579 (2018).